CONF-840604--7

NOTICE

PORTIONS OF THIS REPORT ARE ILLEGIBLE. It has been reproduced from the best available copy to permit the broadest possible availability.

NONEQUILIBRIUM SEGREGATION AND PHASE INSTABILITY IN ALLOY FILMS DURING ELEVATED-TEMPERATURE IRRADIATION IN A HIGH-VOLTAGE ELECTRON MICROSCOPE*

N. Q. Lam and P. R. Okamoto
Materials Science and Technology Division
Argonne, Illinois 60439

CONF-840604--7

DE84 013423

MAY 1984

DISCLAIMER

*This work was supported by the U.S. Department of Energy.
To be presented at the 12th Symposium on Effects of Radiation on Materials, June 18-20, 1984, Williamsburg, VA.

NONEQUILIBRIUM SEGREGATION AND PHASE INSTABILITY IN ALLOY FILMS DURING ELEVATED-TEMPERATURE IRRADIATION IN A HIGH-VOLTAGE ELECTRON MICROSCOPE*

N. Q. Lam and P. R. Okamoto
Materials Science and Technology Division
Argonne, Illinois 60439

ABSTRACT: The effects of defect-production rate gradients, caused by the radial nonuniformity in the electron flux distribution, on solute segregation and phase stability in alloy films undergoing high-voltage electron-microscope (HVEM) irradiation at high temperatures are assessed in the present work. Two-dimensional (axially symmetric) compositional redistributions were calculated, taking into account both axial and transverse radial defect fluxes. It was found that when highly focused beams were employed radiation-induced segregation consisted of two stages: dominant axial segregation at the film surfaces at short irradiation times and competitive radial segregation at longer times. The average alloy composition within the irradiated region could differ greatly from that irradiated with a uniform beam, because of the additional atom transport from or to the region surrounding the irradiated zone under the influence of radial fluxes. As a result, damage-rate gradient effects must be taken into account when interpreting in-situ HVEM observations of segregation-induced phase instabilities. The theoretical predictions are compared with experimental observations of the temporal and spatial dependence of segregation-induced precipitation in thin films of Ni-Al, Ni-Ge and Ni-Si solid solutions.

KEY WORDS: Radiation-induced segregation, compositional redistribution, radiation-induced phase instability, radiation effects, point defects, thin films, high-voltage electron microscopy, computer modeling.

*This work was supported by the U.S. Department of Energy.

INTRODUCTION

High-voltage electron microscopes (HVEM) have been useful in the study of radiation effects in materials by providing large atomic displacement rates and in-situ observations of the microstructural evolution. Numerous radiation-induced phenomena, including dislocation loop evolution, void swelling, and phase instabilities, have been investigated with the HVEM. Since the incoming electrons readily penetrate thin specimens, it has generally been assumed that point defects are generated uniformly along the electron path. For this reason, in previous experimental and theoretical HVEM irradiation studies, no attention was paid to the effects of displacement-rate gradients within the irradiated volume. However, since highly focused electron beams are often employed in order to achieve high damage rates, the beam intensity profile in practice is bell-shaped (or gaussian) and, as a result, the defect production is highly nonuniform in the transverse radial direction. Recently, this spatial nonuniformity has been shown to be capable of causing large defect fluxes out of the irradiated zone [1], and hence, radial-segregation effects can be expected to modify previous theoretical predictions of composition modifications of alloys during high-temperature in-situ irradiations in the HVEM [2].

In the present study, we continue to assess the influence of the radial variation in the defect-production rate on segregation-induced phase changes in alloy thin films. Two-dimensional (axially symmetric) compositional redistribution in HVEM-irradiated alloy films was calculated, and phase instabilities predicted on the basis of the calculated local composition modifications were compared with experimental observations of irradiation-induced precipitation of the γ'-phase in three Ni-based alloys: Ni-Al, Ni-Ge and Ni-Si.

CALCULATIONS OF TWO-DIMENSIONAL IRRADIATION-INDUCED SEGREGATION

Axial and radial compositional redistributions in solid-solution thin films were calculated using a kinetic theory of segregation in binary alloys, in conjunction with a new software package for solving convection-diffusion-kinetics problems. For more details on the theoretical model and the calculational procedure, the reader is referred to our previous articles [1,2]. For the sake of brevity, only a summary is given in this section.

Radiation-induced segregation results from a preferential coupling between fluxes of nonequilibrium point defects and solute elements. The theory describes this coupling in a binary alloy A-B by partitioning the defect fluxes into those occurring by exchange with the various alloy components, i.e. via A and B atoms, and the atom fluxes into those taking place via vacancies and interstitials. The fluxes of atoms and defects can then be expressed in terms of concentration gradients, and partial and total diffusion coefficients of all the species present. To obtain the time evolution of atom and defect distributions, a set of coupled partial differential equations involving the divergences of fluxes, and defect production and annihilation terms must be solved for appropriate initial and boundary conditions.

In the present case, since radial diffusion effects are taken into account, the problem involves solving the kinetic equations in two dimensions. The system of equations was solved for a two-dimensional cylindrical foil domain with an outer radius R_0 and an axial half-thickness L (fig. 1). The centerline ($r = 0$) is a line of symmetry, and the central plane ($z = 0$) is a plane of symmetry. At the foil surfaces ($z = \pm L$), it was assumed that no atoms were lost from the system, and the interstitial and vacancy concentrations were maintained at their thermodynamic equilibrium values. At the outer radius ($r = R_0$, with R_0 taken to be 3 μm), the alloy was assumed to be

unperturbed by irradiation. Numerical solutions were obtained with the aid of the software package DISPL2 [3]. Briefly, the numerical method is based on the use of Galerkin's procedure combined with the use of a smooth piecewise quadratic-basis set in order to reduce the system of partial differential equations to a system of ordinary differential equations [4]. The latter system is then solved with a variant of the Argonne National Laboratory version of the GEAR code [5]. A nonuniform mesh was imposed on the spatial domain, and the transient behavior of the system was determined using a specified error tolerance at each time step.

Model calculations were performed for binary alloys representative of concentrated Ni-Al and Ni-Si solid solutions. The basic physical parameters used were tabulated in ref. 1. Essentially, in Ni-Al alloys, Al atoms were assumed to migrate by preferential exchange with vacancies; they thus segregate in the direction opposite to the vacancy flux. In Ni-Si alloys, Si solutes are assumed to move by forming mobile Si-interstitial complexes, owing to a large binding energy between undersized Si and solvent-interstitials. Consequently, Si atoms segregate in the same direction as the interstitial flux. Although both Ni-Al and Ni-Si are precipitating alloys, precipitate formation was not accounted for in the present calculations. However, from the known solubility limits and the calculated solute redistributions, it is possible to predict when and where a phase change will occur in these alloys. No calculations were made for the Ni-Ge system, in which the Ge solute was found to have a binding energy of 0.20 ± 0.04 eV with the vacancy [6], because the present kinetic model does not include solute transport by bound vacancy-solute pairs [2]. Nevertheless, on the basis of existing experimental evidence, the segregation trends in Ni-Ge alloys are expected to be similar to those in Ni-Si alloys, i.e. the solute atoms migrate in the direction of the defect fluxes.

To simulate the nonuniformity of the damage rate in the radial direction, we assume that the electron-beam intensity profile is bell-shaped, defined by

$$K_o(r) = \begin{cases} K_o^{max}\left[1 + \frac{1}{2}\left(\frac{r}{\delta}\right)^2\left(\frac{r}{R} - 3\,\frac{\delta}{R}\right)\right] & 0 < r < \delta \\ \frac{1}{2}\,K_o^{max}\left(\frac{1 - r/R}{1 - \delta/R}\right)^2\left(2 - 3\,\frac{\delta}{R} + \frac{r}{R}\right) & \delta < r < R \end{cases} \qquad (1)$$

where K_o^{max} is the peak-damage rate at the beam center, δ is the position of the inflection point, and R is the beam radius (see fig. 1). In the present study, we have taken $K_o^{max} = 10^{-3}$ dpa/s, R = 1 μm, and $\delta = 0.5$ R.

The influence of radiation-induced internal sinks for point defects on the redistribution of alloy composition was also considered. These sinks were assumed to be dislocations. Initially, the foil contained $\rho_o = 10^7$ dislocations/cm^2, typical of annealed samples. During irradiation, new dislocations were created within the irradiated zone. Their density depended on space, according to the damage-rate profile described by eq. (1). The peak density was allowed to build up linearly with time, attaining a saturation level ρ^{max} after an irradiation time t^*:

$$\rho(r=0) = \begin{cases} \rho_o + (\rho^{max} - \rho_o)t/t^* & \text{for } t < t^* \\ \rho^{max} & \text{for } t > t^* \end{cases} \qquad (2)$$

In the present calculations, we have chosen $t^* = 3.6 \times 10^3$ s and $\rho^{max} = 10^{10}$ dislocations/cm^2. If no internal sinks are produced by irradiation, $\rho^{max} = \rho_o = 10^7$ dislocations/cm^2.

EXPERIMENTAL PROCEDURE

Most of the Ni-Al, Ni-Ge and Ni-Si alloys used in the present work were kindly provided by Dr. A. Barbu of Centre d'Etudes Nucléaires de Saclay, France. They were prepared from high-purity metals by conventional arc melting. Transmission-electron-microscope discs (255 μm thick and 3 mm in diameter) cut from rolled materials were metallographically polished to obtain optically flat surfaces, solution annealed in an argon-filled quartz capsule at 1000°C for 6 hours, and water-quenched without breaking the capsule. The discs were then jet-polished using the standard technique.

The specimens were irradiated with 1-MeV electrons at various temperatures in the high-voltage electron microscope at Argonne National Laboratory. The electron beam was focused to a ~2 μm-diameter spot size. The maximum current density employed in these irradiations varied from 8.2 to 13.7 A/cm^2. Using a displacement energy of 33 eV and the tabulated cross section for Ni [7], the peak-damage rate, K_o^{max}, was calculated to be between 1×10^{-3} and 1.7×10^{-3} dpa/s.

THEORETICAL PREDICTIONS AND EXPERIMENTAL OBSERVATIONS

Segregation and Phase Instability in Ni-Al Alloys

Segregation Behavior. The time evolution of the calculated surface Al concentration in the center of the irradiated area, $C_{Al}(L,0)$, and the concentration at the foil center, $C_{Al}(0,0)$, is shown in fig. 2 for a 0.4 μm foil of Ni-7 at.% Al alloys irradiated at various temperatures. No radiation-induced sinks were taken into account. In general, after a relatively short irradiation time, large defect fluxes to the foil surfaces occur; consequently, Al depletion takes place there (as illustrated by the dashed curves) due to a preferential transport of Al atoms away from the surface by

vacancies. With increasing time, Al depletion extends deeper into the foil, and $C_{Al}(L,0)$ approaches a minimum, quasi-steady-state value, which is identical to the steady-state value in the case of segregation under uniform irradiation. The extensive solute depletion near the surfaces leads to a moderate increase in $C_{Al}(0,0)$. As the irradiation continues, radial segregation, resulting from defect concentration gradients in the radial direction, becomes competitive with the axial segregation. A large number of point defects migrate in the r-direction, from the peak-damage region transversely into the bulk of the foil. The flow of vacancies generates a net flux of Al atoms in the opposite direction, giving rise to additional Al enrichment in the foil center at the expense of Al depletion in regions surrounding the irradiated volume. As a result, $C_{Al}(0,0)$ increases to a large steady-state value, which is far greater than the corresponding value attained under uniform irradiation conditions. At steady state, $C_{Al}(L,0)$ returns to the initial composition, owing to a large flux of Al atoms to the suface induced by the substantial increase in $C_{Al}(0,0)$.

Radiation-induced segregation is most efficient around 600°C. This temperature dependence can be understood in terms of vacancy mobility and concentration [8-12]. Similar to the case of uniform irradiation, the lower the temperature, the longer the incubation time for segregation, and the greater the time required to achieve steady state. However, the buildup times to steady state calculated here are several orders of magnitude longer than those obtained in the absence of radial defect gradients. This indicates that for the duration of typical in-situ HVEM irradiation experiments (i.e., $t \lesssim 4 \times 10^4$s), steady-state segregation will rarely be attained if highly-focused electron beams are employed.

Figure 3 shows the dependence of segregation on the density of internal sinks. Here, the time evolution of $C_{Al}(L,0)$ and $C_{Al}(0,0)$ in a 0.4 μm foil of Ni-10 at.% Al alloys irradiated at 700°C is plotted for two values of ρ^{max}, 10^7 and 10^{10} dislocations/cm^2, representing two extreme cases. The larger the dislocation density, the smaller the segregation. This can be ascribed to lower local concentrations of defects and small defect gradients as a result of large defect annihilation at internal sinks. Although the buildup time to steady state is virtually the same for both cases, the steady-state $C_{Al}(0,0)$ is considerably larger for $\rho^{max} = 10^7$ cm^{-2} than for $\rho^{max} = 10^{10}$ cm^{-2}, because the smaller the defect concentration gradients, the lower the defect fluxes out of the irradiated zone.

Similar to the effect of internal-sink density, changes in the film thickness lead to variations in the local defect concentrations and, hence, to different magnitudes of axial and radial defect fluxes. As a consequence, the temporal and spatial evolution of the alloy composition will be affected. The time dependence of $C_{Al}(0,0)$ and $C_{Al}(L,0)$ calculated for a Ni-10 at.% Al alloy irradiated at 700°C is illustrated in fig. 4 for different foil thicknesses. The quasi-steady state of the axial segregation is more evident with thinner foils. Also, the time required for attaining this state decreases with decreasing foil thickness, due to the fact that point defects can annihilate faster at the surfaces of thinner foils. Since the radial defect fluxes are smaller in thinner films, the duration of quasi-steady state for axial segregation is longer, and the steady-state value of $C_{Al}(0,0)$ is smaller in thin films than in thick films. However, for sufficiently thick foils ($2L > 0.4$ μm), the defect concentrations at the foil center are insensitive to foil thickness, and therefore, the evolutions of $C_{Al}(0,0)$ and $C_{Al}(L,0)$ are thickness-independent.

Segregation-induced Precipitation. As mentioned above, phase changes are not explicitly accounted for in the present calculations. However, precipitation of a second phase is expected to occur whenever and wherever segregation causes the local solute concentration to exceed the thermodynamic solubility limit. In the following sections, this temporal and spatial dependence of segregation-induced precipitation is used as a basis for comparing theoretical predictions with experimental observations.

As can be seen in fig. 3, at 700°C, $C_{Al}(0,0)$ in a relatively thick foil of Ni-10 at.% Al surpasses the solubility limit C_{Al}^{ℓ} ~ 11.6 at.% [13] at ~ 10^3 s (for $\rho^{max} = 10^7 cm^{-2}$) and ~ 2×10^3 s (for $\rho^{max} = 10^{10}$ cm^{-2}). Theoretically, this pronounced Al enrichment occuring after the quasi-steady state for axial segregation has passed can only result from the effects of radial segregation. This is demonstrated in fig. 5a, which shows that at 700°C, the maximum Al enrichment attainable under uniform irradiation conditions is 11.2 at.% Al. Consequently, although very efficient at short irradiation times, axial segregation alone cannot induce precipitation of the Ni_3Al phase in a Ni-10 at.% Al alloy irradiated 700°C. In order to verify this experimentally, an alloy of this compositon was irradiated at 700°C with a broad beam (2R ~ 10 μm) adjusted to obtain a nearly uniform peak-damage rate of ~ 10^{-3} dpa/s over a 5-μm diameter area of the sample. As shown in fig. 5b, precipitation of the γ'-Ni_3Al did not occur under these conditions for irradiation times less than 3.7×10^3 s. However, as illustrated in fig. 6, when the same alloy was irradiated under similar conditions using a highly focused beam, precipitation of coherent γ' particles occurred after ~900 s of irradiation. They first appeared near the center of the beam, then gradually spread outward to fill the entire irradiated area. It is noted that the

precipitates were not distributed uniformly in the axial direction, but were concentrated near the midplane of the foil, where the Al enrichment is greatest. The observed incubation time of 900 s is in good agreement with that calculated in fig. 3 for the low-dislocation-density case.

In order to investigate the effects of temperature, an adjacent area of the same TEM specimen was irradiated without changing the beam conditions, after reducing the temperature to 500°C where C^{ℓ}_{Al} = 10.2 at.% Al. After a short incubation time of ~ 120 s, γ' precipitates appeared within the irradiated area. As shown in fig. 7, they were much smaller, and their number densities much larger than those observed at 700°C. Since the alloy composition is nearly equal to the solubility limit at 500°C, precipitation in this case can result from axial segregation alone. This is demonstrated in fig. 8 where the temperature dependence of axial segregation is shown for a Ni-10 at.% Al alloy. For example, the calculated incubation time for an irradiation performed at 500°C is ~ 300 s, which is consistent with the experimentally observed value of 120 s.

Now, if the alloy composition is changed, e.g. from 10 to 7 at.% Al, the segregation behavior at 500°C will be different, because the Al concentration is far below C^{ℓ}_{Al}. Axial segregation alone is insufficent to induce precipitation. However, with the influence of radial segregation, $C_{Al}(0,0)$ can be increased to levels above C^{ℓ}_{Al} after ~ 1.5×10^4 - 2.2×10^4 s depending on the density of irradiation-induced dislocations, as shown in fig. 9. Precipitation can therefore ensue in the central regions after a long incubation time. This prediction is in qualitative agreement with the experimental results given in fig. 10. In Ni-7 at.% Al alloys, dislocations were observed to dynamically form in the beam center and move rapidly to the periphery of the irradiated area, forming a dislocation wall. Coherent γ' particles formed

in the central region of the irradiated zone only after ~ 2.4×10^4 s of irradiation, which is consistent with the calculated incubation time for $\rho^{max} = 10^{10}$ cm^{-2}. However, in a number of cases, some γ' preciptates were observed to form earlier in the region of the dislocation walls. These precipitates may be due to local enrichment between dislocations acting as defect sinks.

Segregation and Phase Instability in Ni-Si Alloys

Segregation Behavior. Unlike the case of Ni-Al alloys, in Ni-Si solid solutions, the preferential association of solvent-interstitials with Si solutes results in a disproportionate transport of Si in the direction of the defect flux. The time evolution of $C_{Si}(0,0)$ and $C_{Si}(L,0)$ in a 0.4 μm foil of a Ni-9.5 at.% Si alloy irradiated at 600°C is shown in fig. 11. Axial segregation occurs first as a result of efficient annihilation of point defects at the surfaces; the surface is quickly enriched in Si. The concentration $C_{Si}(L,0)$ increases rapidly, reaching a quasi-steady-state value of ~ 66 at.% at ~10^3 s. If the irradiation were uniform throughout the foil, this quasi-steady state would be true steady state, at which the Si concentrations at the surface and center correspond to those indicated by the dotted lines. For $t \gtrsim 10^3$ s, the effect of radial defect fluxes is noticeable; Si atoms are transported out of the irradiated zone in the radial direction, causing Si enrichment in regions surrounding this zone [1]. The enrichment becomes more and more apparent with increasing time, at the expense of severe Si depletion in the central region; $C_{Si}(0,0)$ decreases to practially zero. This depletion, in turn, induces back-diffusion of Si from the surface region into the foil center, reducing $C_{Si}(L,0)$ monotonically to smaller values at $t > 4 \times 10^3$ s. The effects of irradiation temperature, film thickness and irradiation-induced

dislocations on the segregation kinetics are similar to the above case of Ni-Al alloys.

Segregation-induced Precipitation. As can be seen in fig. 11, the calculated Si concentration at the foil surface, $C_{Si}(L,0)$, exceeds the solubility limit, C^{ℓ}_{Si} = 10.2 at.% [14] after a very short irradiation time, t ≈ 0.2 s. Thus, a film of the γ'-Ni_3Si phase can be expected to form almost instantly. It should appear first at the center of the beam where the defect fluxes are greatest, then grow radially outward to cover the entire irradiated area. Various stages of the film growth process observed during the irradiation of a Ni-9.5 at.% Si alloy at 700°C are shown in fig. 12. The growing films appeared as dark circular zones in bright-field images taken with 220-matrix reflections. Figure 11 also indicates that the Si concentration at the surface gradually decreases after ~ 4 x 10^3 s of irradiation. This effect of radial segregation may lead to a gradual dissolution of the γ' surface film. In fact, electron diffraction patterns taken during irradiation showed that superlattice reflections became weak and eventually dissappeared after long irradiation times. However, since the intensity of superlattice reflections decreases very rapidly with increasing deviations from the exact Bragg condition, particularly in thick foils, the gradual smearing out of the superlattice reflections may be due to the very high dislocation densities which develop in Ni-Si alloys.

Figure 12 also shows that a ring of γ' particles forms outside the irradiated area (marked by arrows). This ring is a characteristic feature of irradiations carried out with highly focused beams, and is due to the effects of radial segregation. The Si enrichment outside the irradiated zone results from the radial outflow of defects from the damage zone which induces a corresponding outflow of Si atoms. The γ' ring was observed to move outward; for

example, its inner radius increased from ~ 1.6 μm to ~ 2.4 μm when the irradiation time increased from 900 s to 3.6×10^3 s.

Segregation and Phase Instability in Ni-Ge Alloys

In recent studies, precipitation of the γ'-Ni_3Ge phase was observed at sinks in Ni-Ge alloys [15-17]. It was found that the radiation-induced segregation behavior in this system was generally similar to that in Ni-Si alloys. We therefore expect that under highly-focused beam conditions, axial segregation leading to Ge enrichment at the foil surfaces will dominate at short irradiation times and that radial segregation, i.e., preferential transport of Ge out of the irradiated zone will dominate at longer times. Moreover, because the dislocation densities produced in the irradiated zones of Ni-Ge alloys are generally much lower than in Ni-Si alloys, the effects of radial segregation can be more dramatic, and, as a result, the transient nature of axial segregation is more evident in this system than in Ni-Si alloys. A particular striking example of the effect in a Ni-10 at.% Ge alloy irradiated at 600°C is shown in fig. 13. Initially, due to the effects of axial segregation, a γ'-Ni_3Ge precipitate film formed and grew rapidly on the foil surfaces. However, after reaching a maximum thickness at t ≈ 600 s, the surface film dissolved into the matrix presumably under the influence of radial segregation. The film disappeared completely after ~ 2.4×10^3 s of irradiation. It is noted that a ring of γ'-particles was observed rather early in time, after ~ 300 s, on the edges of the irradiated region, and shrank to disappearance at the same time with the surface film. This ring effect was much more pronounced when the beam diameter was reduced, as shown in fig. 14. In Ni-6 at.% Ge alloys irradiated at the same temperature, surface γ' films were not observed, only γ' particles appeared in the sub-

surface regions. They also dissolved completely after ~ 2.4×10^3 s, as in the case of Ni-10 at.% Ge alloys. This rapid dissolution of the γ' precipitates observed in these alloys cannot be interpreted at present on the basis of recent tracer-diffusion measurements, which indicate that the activation enthalpy for Ge diffusion in Ni is not too different from that for self-diffusion [18]. Further study will be needed in order to fully understand the segregation kinetics in this system.

CONCLUDING REMARKS

The present theoretical predictions and experimental demonstrations of complex kinetics of segregation that occurs in alloy films may provide useful information in connection with the understanding of high-dose HVEM irradiation-induced processes at elevated temperatures. The drastic modifications of the alloy composition, and hence, phase destabilization, in the irradiated zone must be taken into account in any analysis of property changes after a long high-temperature HVEM irradiation. For example, current theoretical models of radiation-induced precipitation in undersaturated solid solutions [19] are based largely on results of in-situ HVEM irradiation experiments carried out with highly-focused electron beams. Because the effects of damage-rate gradients were not recognized at the time, the interpretation of the observed kinetics, in particular, the temperature and dose-rate dependences, need to be reassessed.

Finally, these predictions of segregation-driven phase instability may also be generalized to complex alloy systems, such as austenitic Fe-Cr-Ni alloys. In fact, similar to the compositional evolution in the peak-damage region of a proton-irradiated Fe-Cr-Ni sample [20], severe Ni depletion will take place in the foil center as a consequence of radial segregation during

HVEM irradiation. The local alloy composition is effectively shifted towards the α-field of the phase diagram, i.e. an austenite-to-ferrite transformation is highly favored in the central region. Thus, after a long HVEM irradiation, the irradiated zone will consist of a relatively thick layer of ferrite embedded in the austenite phase.

ACKNOWLEDGMENTS

We wish to thank G. K. Leaf and M. Minkoff for their collaboration in the early phase of the theoretical modeling, and A. Barbu of CEN-Saclay for kindly providing us with alloys used in the present study. We are also grateful to B. J. Kestel and E. A. Ryan for their valuable assistance in the experiments.

REFERENCES

[1] Lam, N. Q., Leaf, G. K. and Minkoff, M., Journal of Nuclear Materials, Vol. 118, 1983, pp. 248-259.

[2] Wiedersich, H., Okamoto, P. R. and Lam, N. Q., Journal of Nuclear Materials, Vol. 83, 1979, pp. 98-108.

[3] Leaf, G. K. and Minkoff, M., in Advances in Computer Methods for Partial Differential Equations - IV, R. Vichnevetsky and R. S. Stepleman, Ed., International Association for Mathematics and Computers in Simulation, Rutgers University, New Jersey, 1981, p. 343.

[4] Leaf, G. K., Minkoff, M., Byrne, G. D., Sorensen, D., Bleakney, T. and Saltzman, J., "DISPL: A Software Package for One and Two Spatially Dimensioned Kinetics-Diffusion Problems", Report ANL-77-12, Rev. 1, Argonne National Laboratory, Argonne, Illinois, 1978.

[5] Hindmarsh, A., "GEAR: Ordinary Differential Equation System Solver", Report UCID-30001, Lawrence Livermore Laboratory, Livermore, California, 1974.

[6] Smedskjaer, L. C., Fluss, M. J., Legnini, D. G., Chason, M. K. and Siegel, R. W., in Positron Annihilation, P. G. Coleman et al., Ed., North-Holland Publishing Company, Amsterdam, 1982, pp. 526-528.

[7] Oen, O.S., in Cross Sections for Atomic Displacements in Solids by Fast Electrons, ORNL Report No. 4897, Oak Ridge National Laboratory, Oak Ridge, Tennessee, 1973.

[8] Johnson, R. A. and Lam, N. Q., Physical Review B, Vol. 13, 1976, pp. 4364-4375; Journal of Nuclear Materials, Vol. 69 & 70, 1978, pp. 424-433.

[9] Lam, N. Q., Okamoto, P. R., Wiedersich, H. and Taylor, A., Metallurgical Transactions, Vol. 9A, 1978, pp. 1707-1714.

[10] Lam, N. Q., Okamoto, P. R. and Wiedersich, H., Journal of Nuclear Materials, Vol. 74, 1978, pp. 101-113.

[11] Wiedersich, H., Okamoto, P. R. and Lam, N. Q., in Radiation Effects in Breeder Reactor Structural Materials, M. L. Bleiberg and J. W. Bennett, Ed., The Metallurgical Society of AIME, New York, 1977, pp. 801-819.

[12] Wiedersich, H. and Lam, N. Q., in Phase Transformations During Irradiation, F. V. Nolfi, Jr., Ed., Applied Science Publishers, Barking, England, 1983, pp. 1-46.

[13] Ardell, A. J. and Nicholson, R. B., Acta Metallurgica, Vol. 14, 1966, pp. 1295-1309.

[14] Rastogi, P. K. and Ardell, A. J., Acta Metallurgica, Vol. 19, 1971, pp. 321-330.

[15] Barbu, A. in Irradiation Behavior of Metallic Materials for Fast Reactor Core Components, J. Poirier and J. M. Dupouy, Ed., Commissariat à l'Energie Atomique, Gif-sur-Yvette, France, 1979, pp. 69-73.

[16] Gupta, R. P. and Lam, N. Q., Scripta Metallurgica, Vol. 13, 1979, pp. 1005-1010.

[17] Rehn, L. E. and Okamoto, P. R. in Phase Transformations During Irradiation, F. V. Nolfi, Jr., Ed., Applied Science Publishers, Barking, England, 1983, pp. 247-290.

[18] Mantl, S., Rothman, S. J., Nowicki, L. J. and Lerner, J. L., Journal of Physics F: Metal Physics, Vol. 13, 1983, pp. 1441-1448.

[19] Martin, G., Cauvin, R. and Barbu, A., in Phase Transformations During Irradiation, F. V. Nolfi, Jr., Ed., Applied Science Publishers, Barking, England, 1983, pp. 47-74.

[20] Lam, N. Q., Journal of Nuclear Materials, Vol. 117, 1983, pp. 106-112.

FIGURE CAPTIONS

Fig. 1. Schematic description of the cylindrical foil domain considered and the spatial distribution of defect-production rates.

Fig. 2. Time dependence of $C_{Al}(0,0)$ and $C_{Al}(L,0)$ in a 0.4 μm thick foil of a Ni-7 at.% Al alloy irradiated at various temperatures.

Fig. 3. Time dependence of $C_{Al}(0,0)$ (solid curves) and $C_{Al}(L,0)$ (dashed curves) in a 0.4 μm foil of a Ni-10 at.% Al alloys calculated for T = 700°C and two values of ρ^{max}, 10^7 and 10^{10} dislocations/cm^2. The thin horizontal line represents the Al solubility limit.

Fig. 4. Time evolution of $C_{Al}(0,0)$ (solid curves) and $C_{Al}(L,0)$ (dashed curves) in Ni-10 at.% Al alloy films of different thicknesses. $\rho^{max} = 10^{10}$ dislocations/cm^2. The thin horizontal line represents the Al solubility limit.

Fig. 5(a) Time evolution of the Al concentrations at the center (solid curves) and surface (dashed curves) of Ni-10 at.% Al alloy films of different thicknesses under uniform irradiation with $K_o = 10^{-3}$ dpa/s at 700°C. No internal sink was assumed. The thin horizontal line indicates the Al solubility limit.

Fig. 5(b) Bright-field micrographs showing microstructural changes in a Ni-10 at.% Al alloy irradiated at 700°C. Irradiation parameters: 2R = 10 μm, $K_o^{max} = 10^{-3}$ dpa/s, $\vec{n} \sim [100]$ and $\vec{g} = [220]$. The irradiation times are indicated. Note the absence of γ' particles.

Fig. 6. Phase instability in a Ni-10 at.% Al film irradiated at 700°C. Irradiation parameters: $2R \simeq 2.2$ μm, $K_o^{max} \simeq 10^{-3}$ dpa/s, $\vec{n} \sim [100]$ and $\vec{g} = [220]$. The irradiation times are indicated.

Fig. 7. (a) Bright-field micrograph showing the distribution of γ' particles in a Ni-10 at.% Al alloy film irradiated at 500°C with a highly focused beam. Irradiation parameters: $2R \simeq 2.2$ μm, $K_o^{max} \simeq 10^{-3}$ dpa/s, $\vec{n} \sim [100]$ and $\vec{g} = [220]$. Note that the density of γ' particles reflects the radial intensity distribution of the electron beam.
(b) Corresponding selected-area-diffraction pattern showing γ' superlattice reflections.

Fig. 8. Temperature and time dependences of the Al concentrations at the center (solid curves) and surface (dashed curves) of a 0.4 μm foil of a Ni-10 at.% Al alloy under uniform irradiation with $K_o = 10^{-3}$ dpa/s. The horizontal arrows indicate the Al solubility limits at various temperatures.

Fig. 9. Time evolution of $C_{Al}(0,0)$ (solid curves) and $C_{Al}(L,0)$ (dashed curves) in a 0.4 μm thick foil of a Ni-7 at.% Al alloy calculated for $T \simeq 500$°C and two values of ρ^{max}, 10^7 and 10^{10} dislocations/cm^2. The thin horizontal line represents the Al solubility limit.

Fig. 10. Bright-field images showing the microstructural evolution in a Ni-7 at.% Al alloy film irradiated at 500°C. Irradiation parameters: $2R = 2.1$ μm, $K_o^{max} = 10^{-3}$ dpa/s, $\vec{n} \sim [100]$ and $\vec{g} = [220]$. The irradiation times are indicated. Precipitation of γ' particles in the central region was observed after ~ 7 hours of irradiation.

Fig. 11. Time dependence of $C_{Si}(0,0)$ and $C_{Si}(L,0)$ in a 0.4 μm foil of a Ni-9.5 at.% Si alloy calculated for T = 600 °C and $\rho^{max} = 10^{10}$ dislocations/cm^2. The dotted lines indicate the corresponding steady-state concentrations in the same foil under uniform irradiation with $K_o = 10^{-3}$ dpa/s. The thin horizontal line represents the Si solubility limit.

Fig. 12. Bright-field images showing various stages in the growth of segregation-induced γ' surface films on a Ni-9.5 at.% Si alloy foil irradiated at 600°C. Irradiation parameters: $2R = 2.1$ μm, $K_o^{max} = 1.6 \times 10^{-3}$ dpa/s, $\vec{n} \sim [100]$ and $\vec{g} = [220]$. The irradiation times are indicated. The dark circular zones are regions of the film that have exceeded the thickness necessary to give rise to Moire fringe effects. The arrows mark the position of a ring of discrete γ' particles resulting from the effects of radial segregation.

Fig. 13. Bright-field images showing various stages in the evolution segregation-induced γ' surface films on a Ni-10 at.% Ge foil irradiated at 600°C. Irradiation parameters: $2R = 2.6$ μm, $K_o^{max} = 1.5 \times 10^{-3}$ dpa/s, $\vec{n} \sim [100]$ and $\vec{g} = [220]$. The irradiation times are indicated. Note the disappearance of surface films after ~ 40 minutes of irradiation.

Fig. 14. Bright-field micrographs showing segregation-induced Ni_3Ge precipitates in a Ni-10 at.% Ge alloy. Irradiation parameters: $2R = 1.2$ μm, $K_o^{max} = 1.6 \times 10^{-3}$ dpa/s, $\vec{n} \sim [110]$, and (a) $\vec{g} = [002]$ and (b) $\vec{g} = [220]$. The dark inner zone is the irradiated area covered by a surface film of Ni_3Ge. The outer circular zone contains a high density of discrete Ni_3Ge particles that result from the radial outflow of Ge from the irradiated zone.

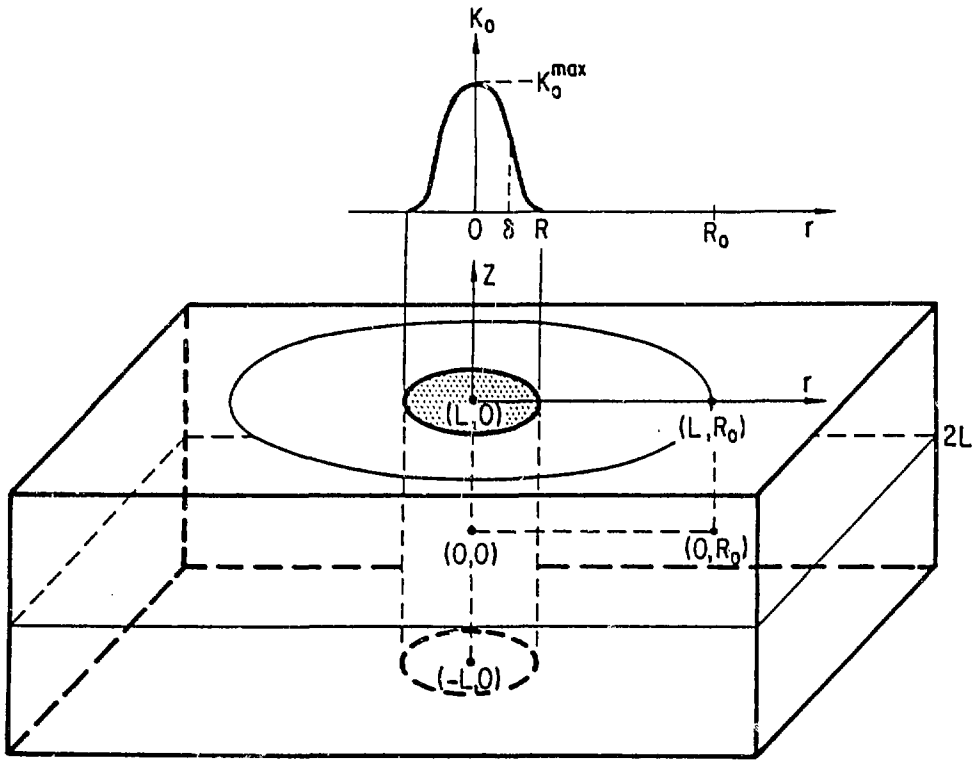

Fig. 1. Schematic description of the cylindrical foil domain considered and the spatial distribution of defect-production rates.

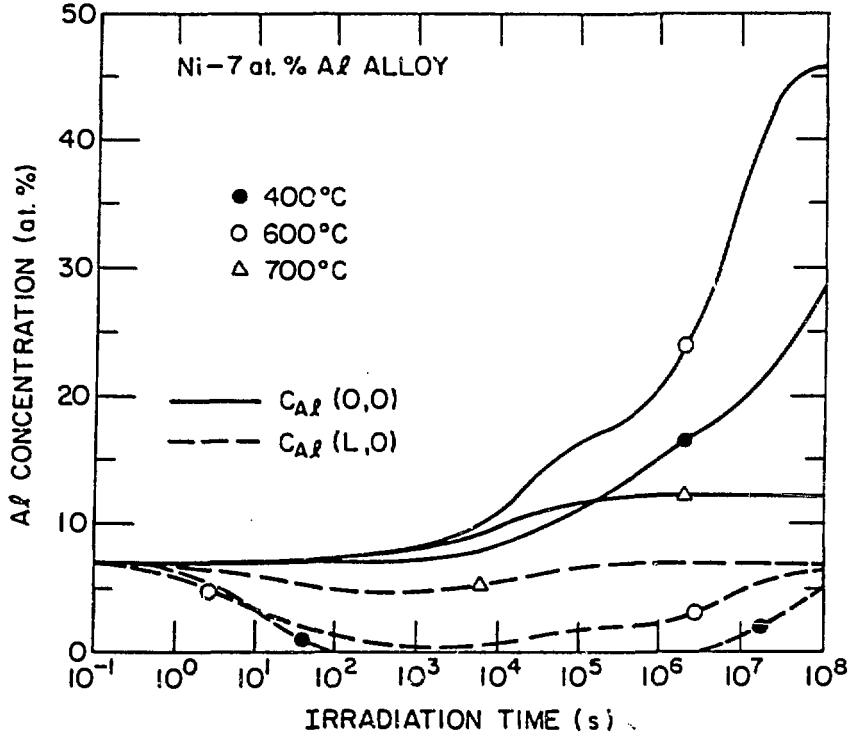

Fig. 2. Time dependence of $C_{Al}(0,0)$ and $C_{Al}(L,0)$ in a 0.4 μm thick foil of a Ni-7 at.% Al alloy irradiated at various temperatures.

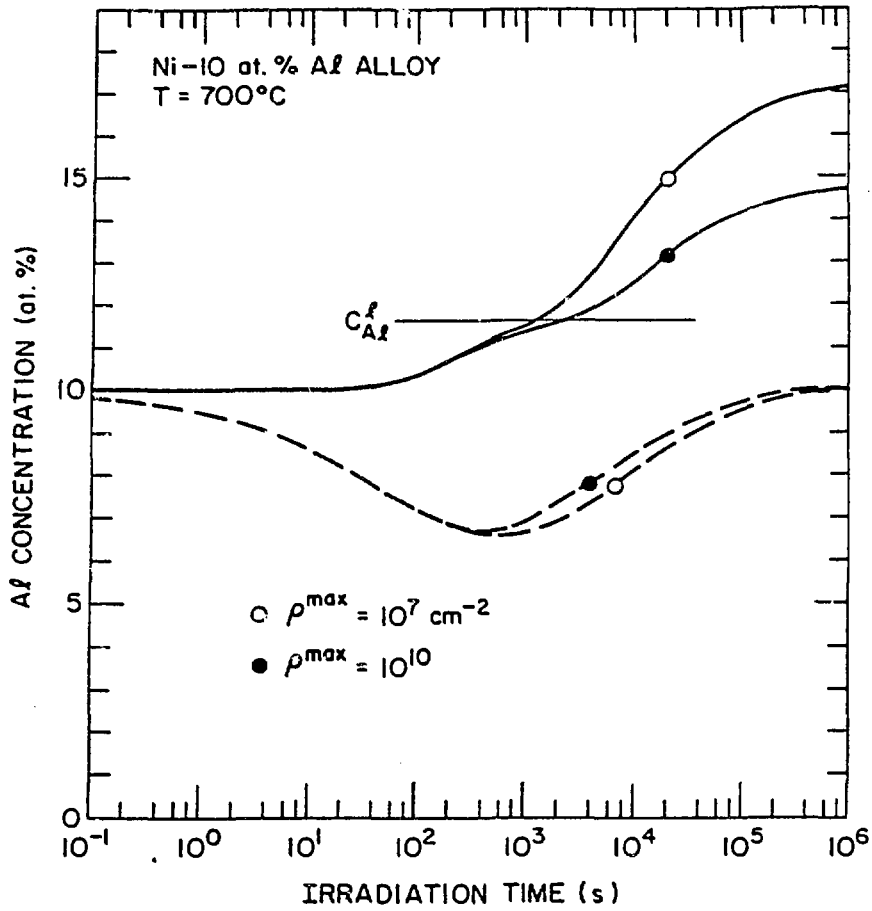

Fig. 3. Time dependence of $C_{Al}(0,0)$ (solid curves) and $C_{Al}(L,0)$ (dashed curves) in a 0.4 μm foil of a Ni-10 at.% Al alloys calculated for T = 700°C and two values of ρ^{max}, 10^7 and 10^{10} dislocations/cm^2. The thin horizontal line represents the Al solubility limit.

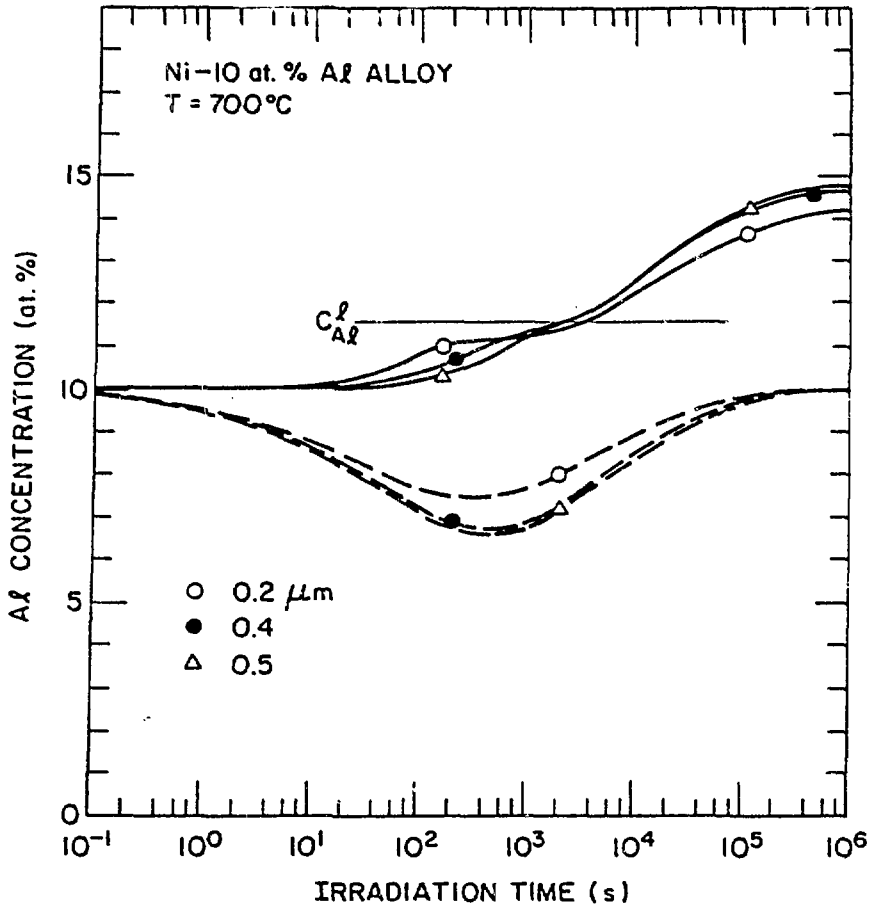

Fig. 4. Time evolution of $C_{Al}(0,t)$ (solid curves) and $C_{Al}(L,0)$ (dashed curves) in Ni-10 at.% Al alloy films of different thicknesses. $\rho^{max} = 10^{10}$ dislocations/cm^2. The thin horizontal line represents the Al solubility limit.

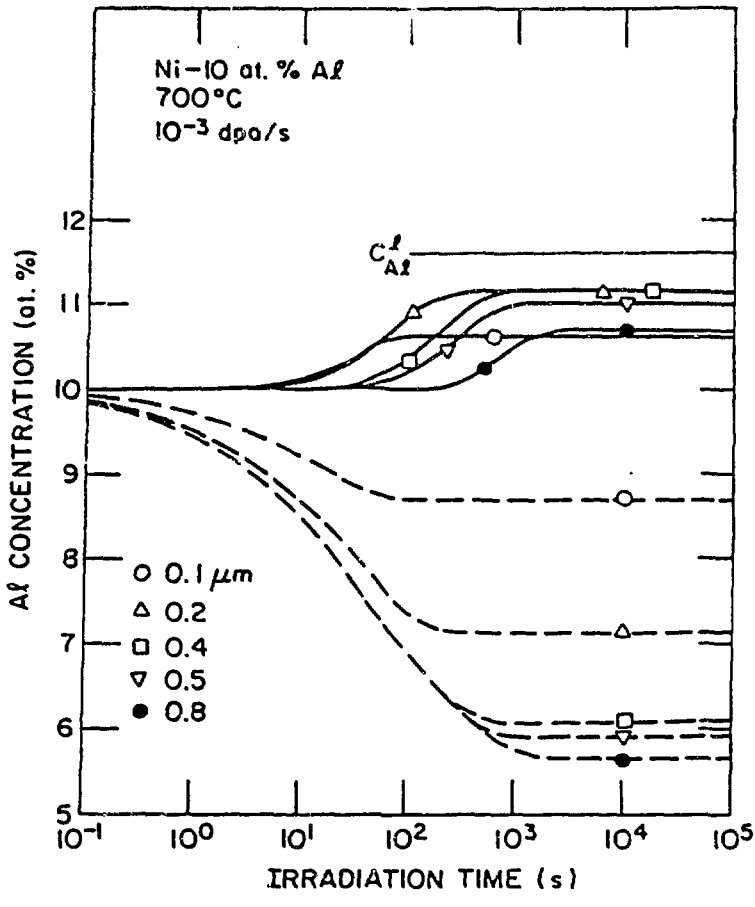

Fig. 5(a) Time evolution of the Al concentrations at the center (solid curves) and surface (dashed curves) of Ni-10 at.% Al alloy films of different thicknesses under uniform irradiation with $K_0 = 10^{-3}$ dpa/s at 700°C. No internal sink was assumed. The thin horizontal line indicates the Al solubility limit.

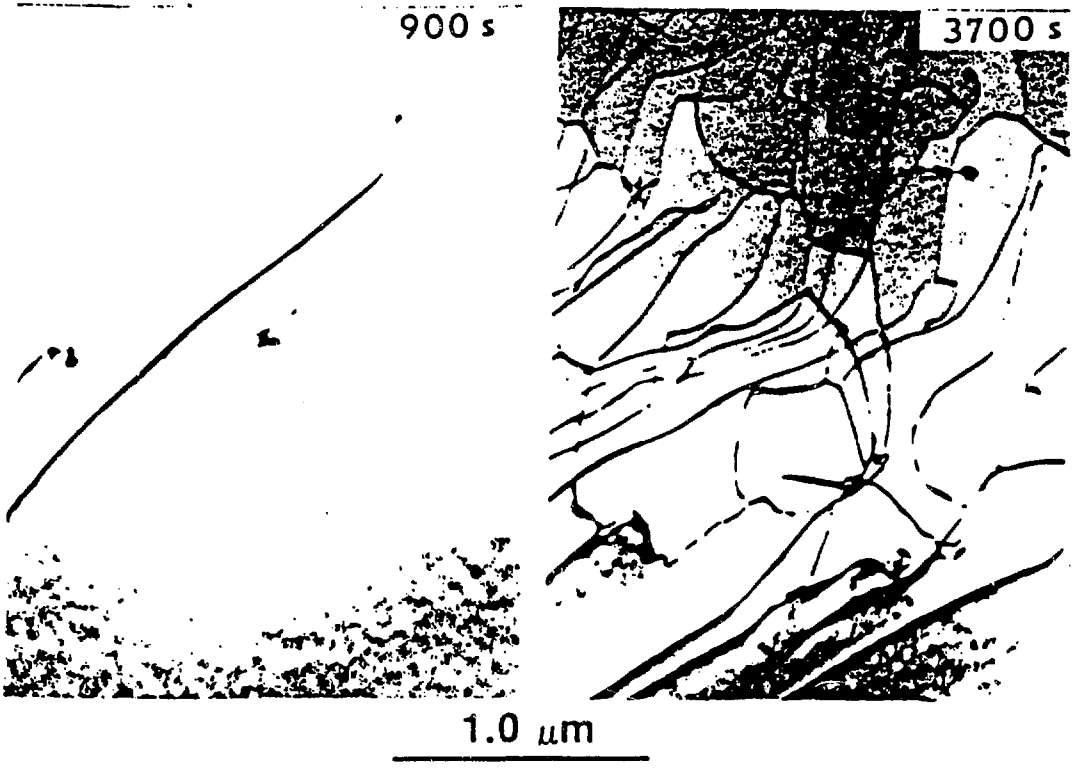

Fig. 5(b) Bright-field micrographs showing microstructural changes in a Ni-10 at.% Al alloy irradiated at 700°C. Irradiation parameters: $2R = 10\ \mu m$, $K_o^{max} = 10^{-3}$ dpa/s, $\vec{n} \sim [100]$ and $\vec{g} = [220]$. The irradiation times are indicated. Note the absence of γ' particles.

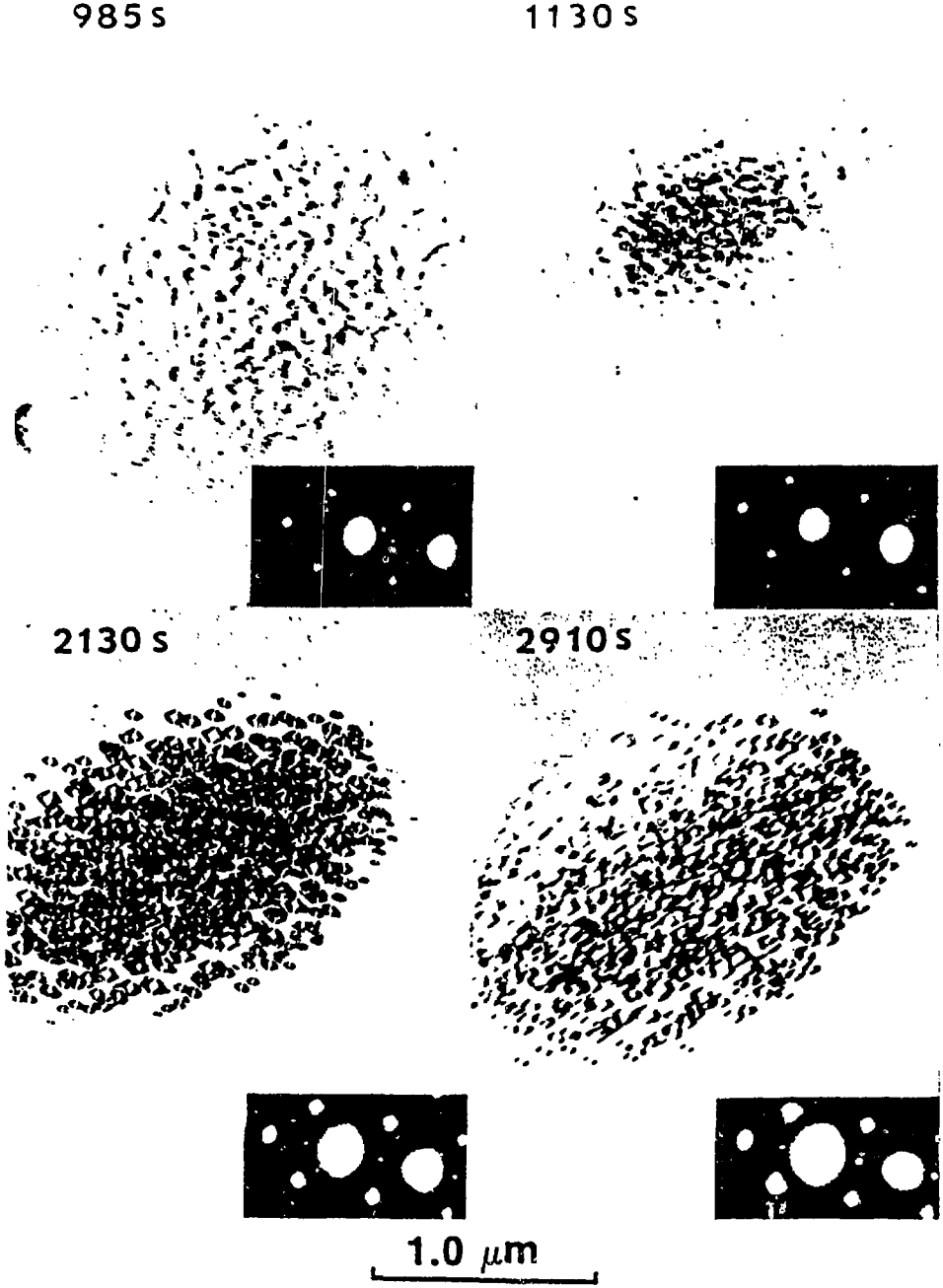

Fig. 6. Phase instability in a Ni-10 at.% Al film irradiated at 700°C. Irradiation parameters: $2R = 2.2$ μm, $K_o^{max} = 10^{-3}$ dpa/s, $\vec{n} \sim [100]$ and $\vec{g} = [220]$. The irradiation times are indicated.

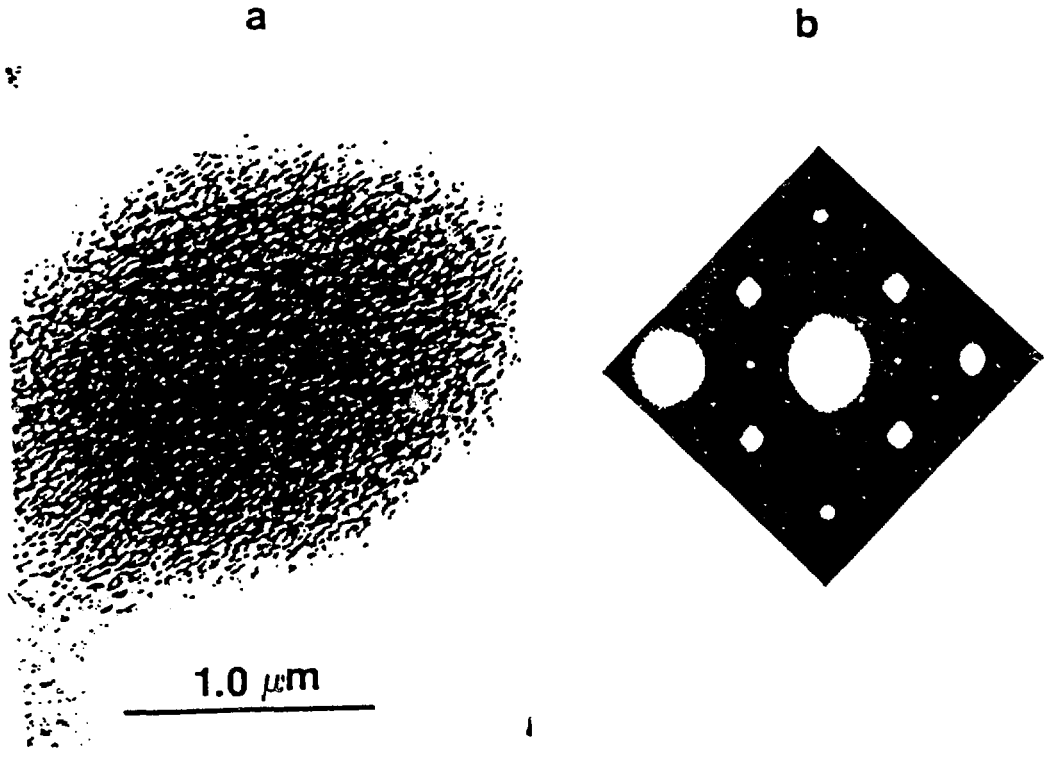

Fig. 7. (a) Bright-field micrograph showing the distribution of γ' particles in a Ni-10 at.% Al alloy film irradiated at 500°C with a highly focused beam. Irradiation parameters: $2R = 2.2\mu m$, $K_o^{max} = 10^{-3}$ dpa/s, $\vec{n} \sim [100]$ and $\vec{g} = [220]$. Note that the density of γ' particles reflects the radial intensity distribution of the electron beam.
(b) Corresponding selected-area-diffraction pattern showing γ' superlattice reflections.

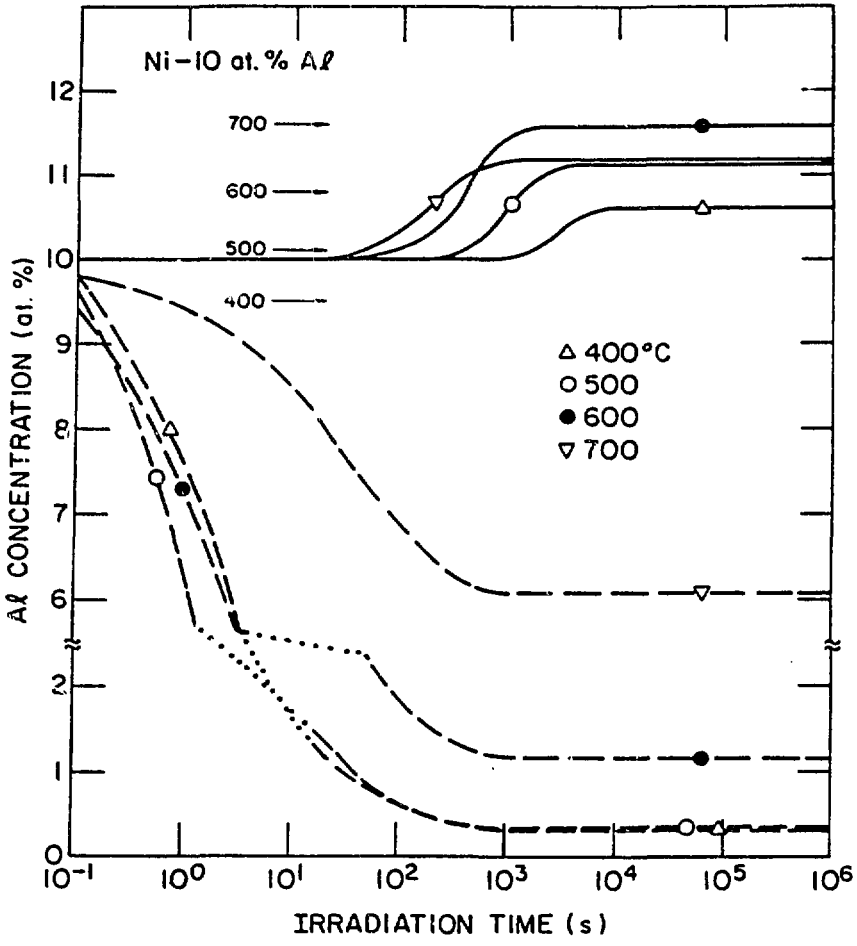

Fig. 8. Temperature and time dependences of the Al concentrations at the center (solid curves) and surface (dashed curves) of a 0.4 μm foil of a Ni–10 at.% Al alloy under uniform irradiation with $K_o = 10^{-3}$ dpa/s. The horizontal arrows indicate the Al solubility limits at various temperatures.

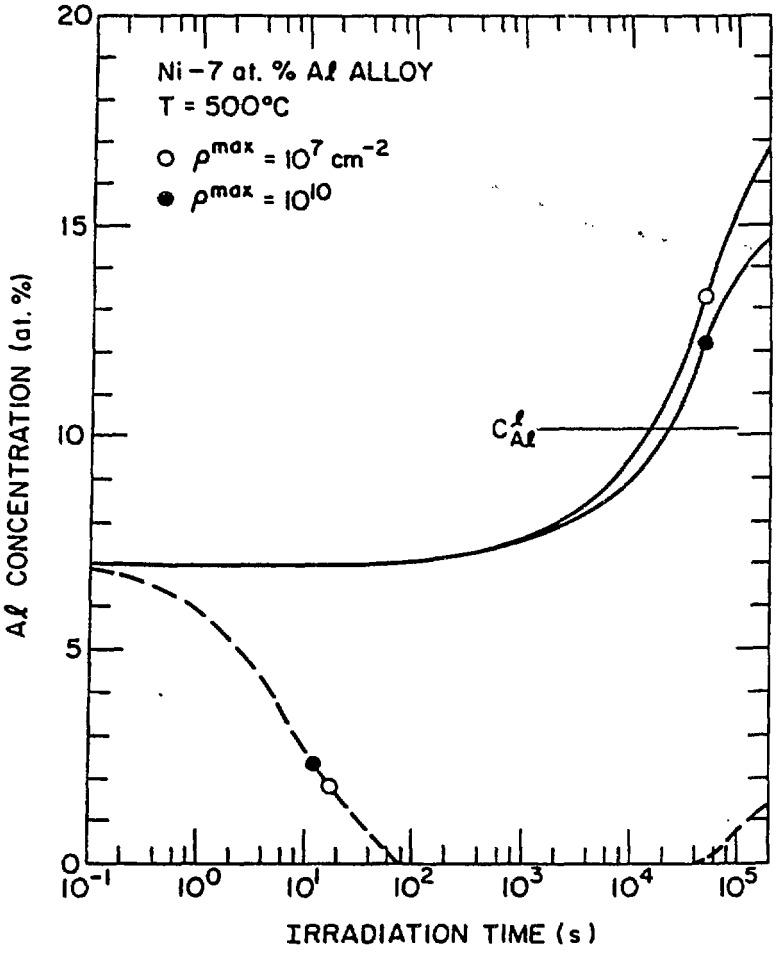

Fig. 9. Time evolution of $C_{Al}(0,0)$ (solid curves) and $C_{Al}(L,0)$ (dashed curves) in a 0.4 μm thick foil of a Ni-7 at.% Al alloy calculated for T = 500°C and two values of ρ^{max}, 10^7 and 10^{10} dislocations/cm^2. The thin horizontal line represents the Al solubility limit.

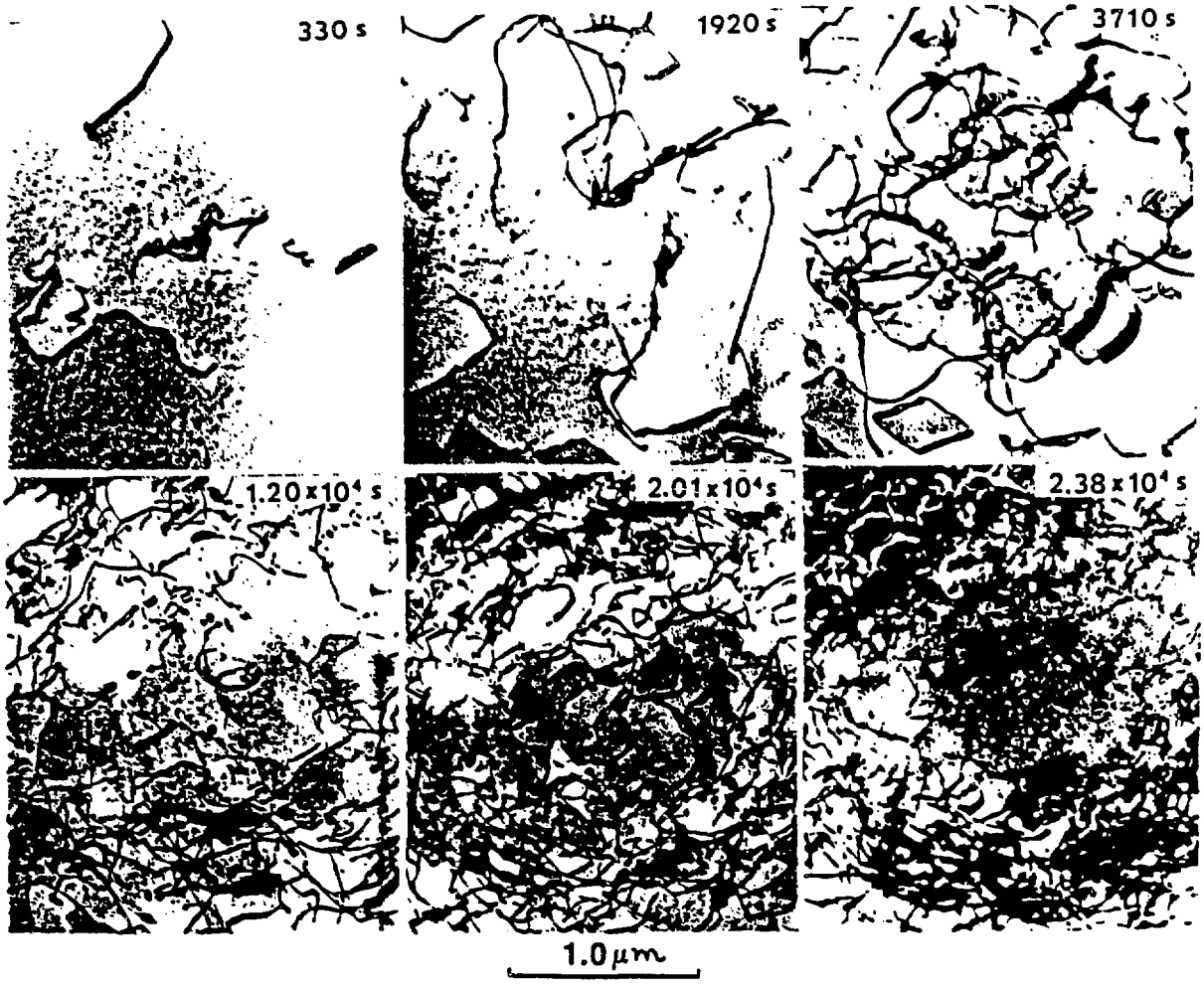

Fig. 10. Bright-field images showing the microstructural evolution in a Ni-7 at.% Al alloy film irradiated at 500°C. Irradiation parameters: $2R = 2.1\ \mu m$, $K_o^{max} = 10^{-3}$ dpa/s, $\vec{n} \sim [100]$ and $\vec{g} = [220]$. The irradiation times are indicated. Precipitation of γ' particles in the central region was observed after ~ 7 hours of irradiation.

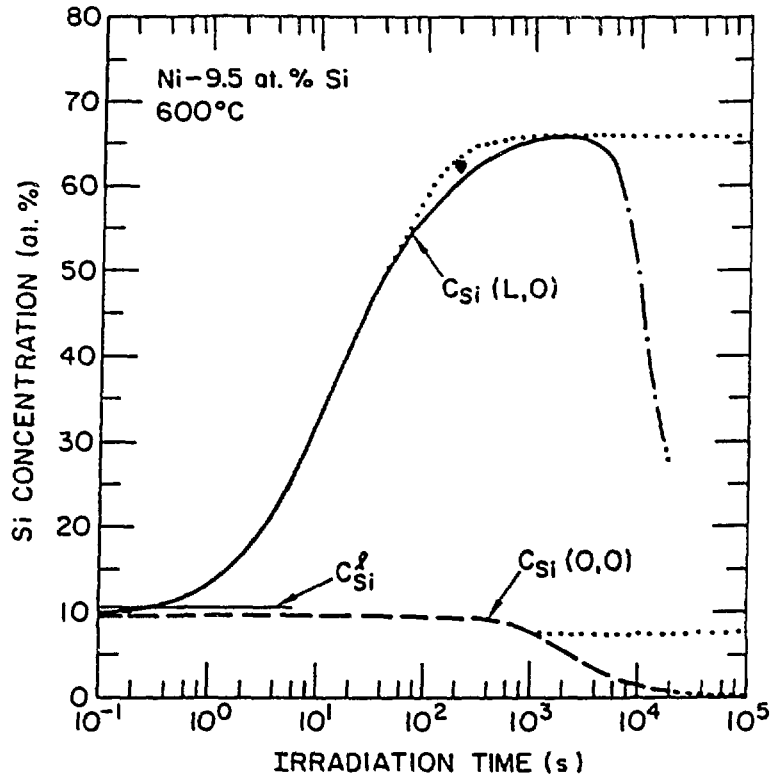

Fig. 11. Time dependence of $C_{Si}(0,0)$ and $C_{Si}(L,0)$ in a 0.4 μm foil of a Ni-9.5 at.% Si alloy calculated for T = 600 °C and $\rho^{max} = 10^{10}$ dislocations/cm^2. The dotted lines indicate the corresponding steady-state concentrations in the same foil under uniform irradiation with $K_o = 10^{-3}$ dpa/s. The thin horizontal line represents the Si solubility limit.

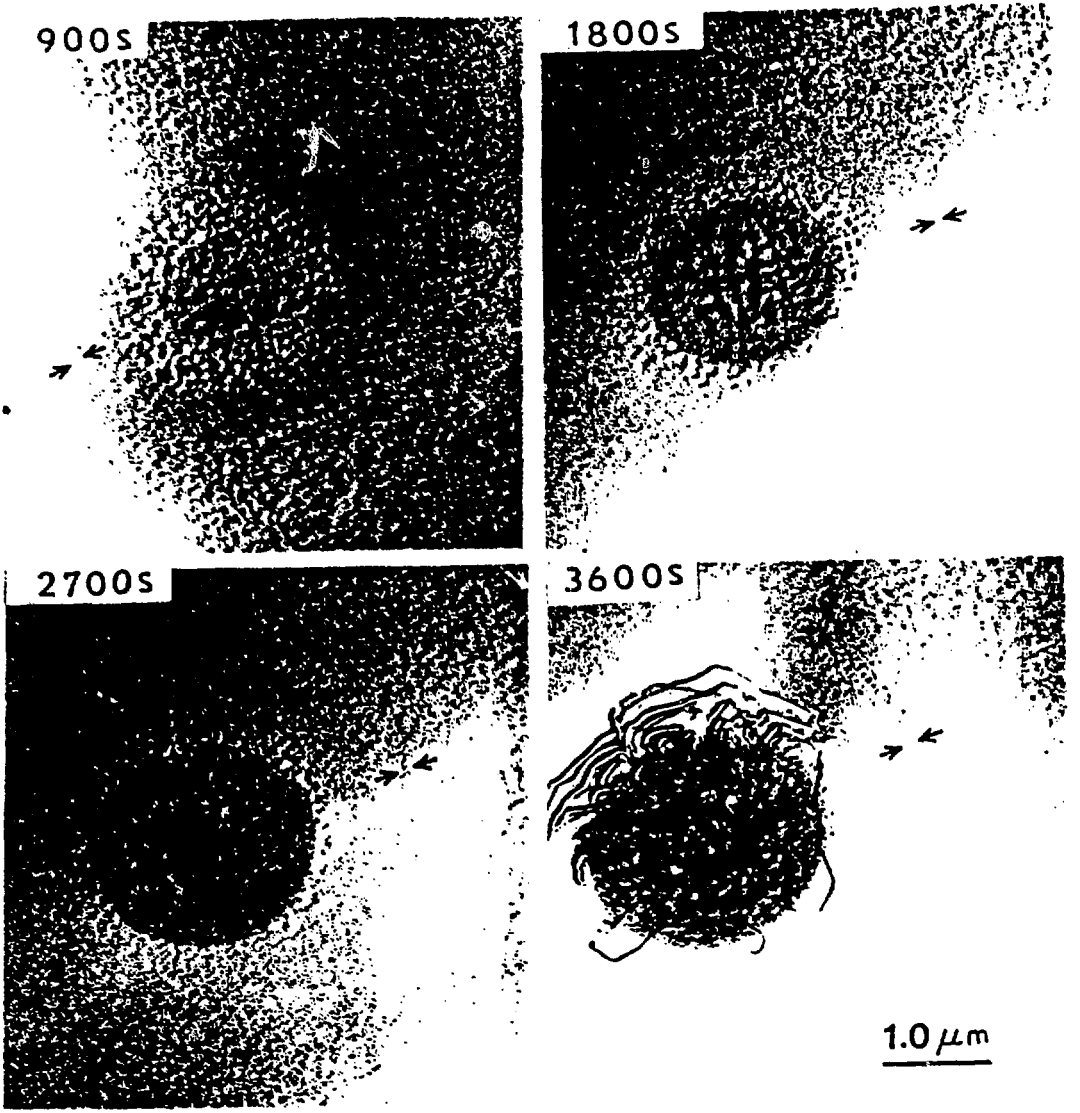

Fig. 12. Bright-field images showing various stages in the growth of segregation-induced γ' surface films on a Ni-9.5 at.% Si alloy foil irradiated at 600°C. Irradiation parameters: 2R = 2.1 μm, $K_o^{max} = 1.6 \times 10^{-3}$ dpa/s, $\vec{n} \sim [100]$ and $\vec{g} = [220]$. The irradiation times are indicated. The dark circular zones are regions of the film that have exceeded the thickness necessary to give rise to Moire fringe effects. The arrows mark the position of a ring of discrete γ' particles resulting from the effects of radial segregation.

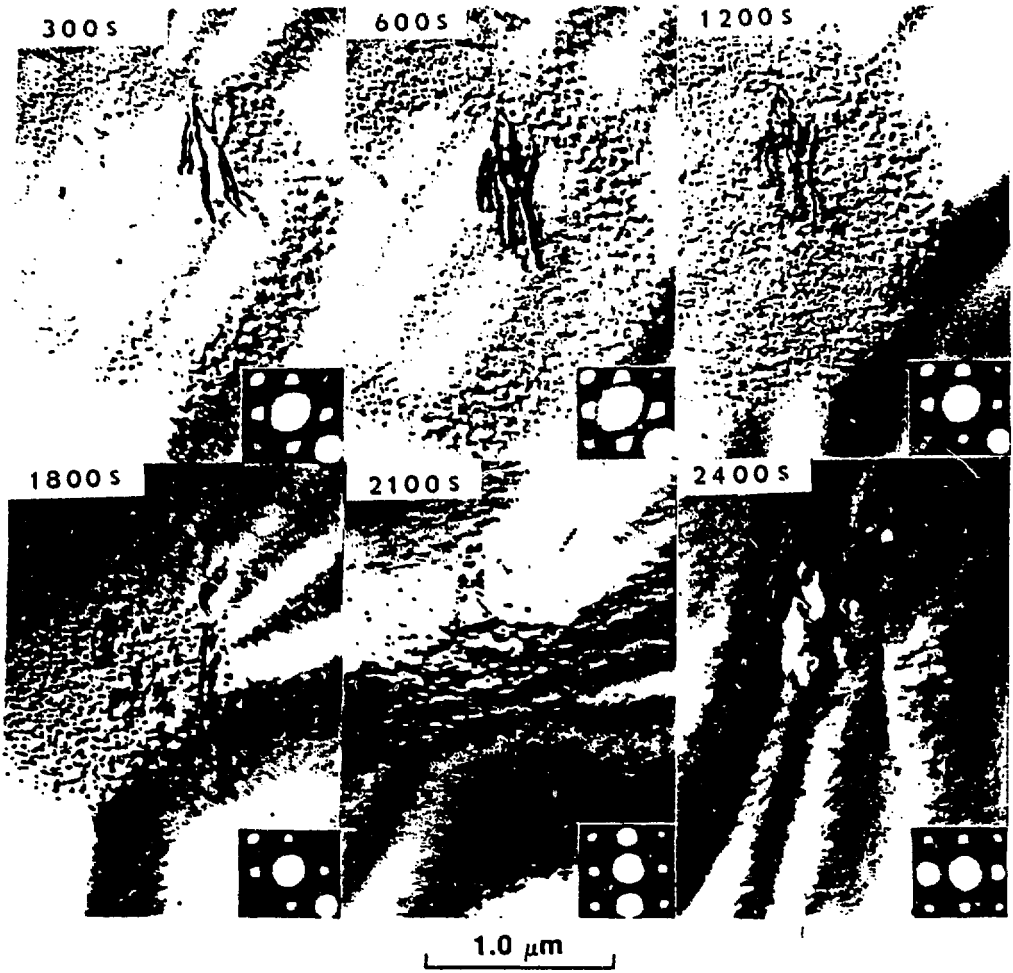

Fig. 13. Bright-field images showing various stages in the evolution segregation-induced γ' surface films on a Ni-10 at.% Ge foil irradiated at 600°C. Irradiation parameters: 2R = 2.6 μm, $K_o^{max} = 1.5 \times 10^{-3}$ dpa/s, $\vec{n} \sim [100]$ and $\vec{g} = [220]$. The irradiation times are indicated. Note the disappearance of surface films after ~ 40 minutes of irradiation.

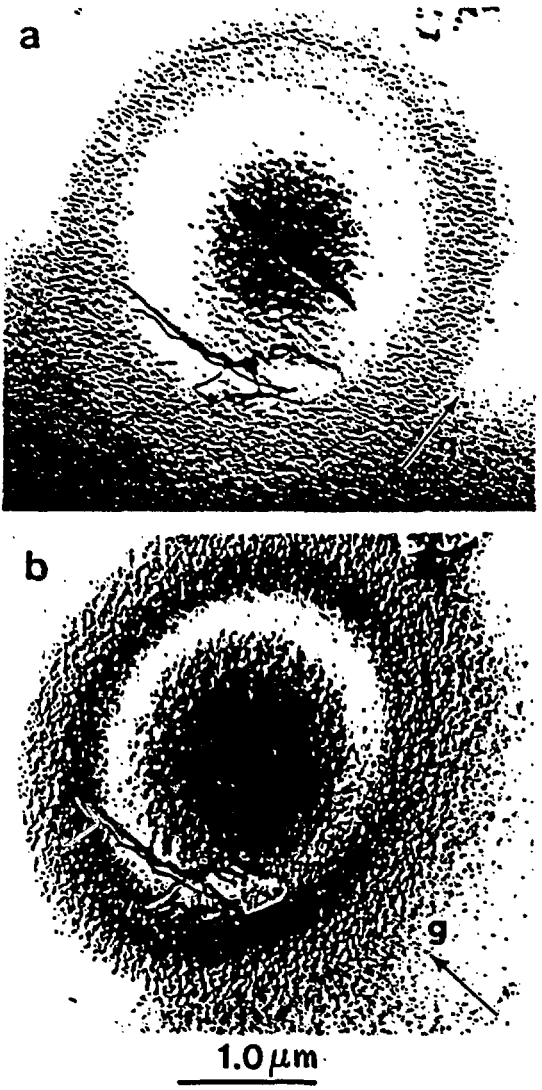

Fig. 14. Bright-field micrographs showing segregation-induced Ni_3Ge precipitates in a Ni-10 at.% Ge alloy. Irradiation parameters: $2R = 1.2$ μm, $K_o^{max} = 1.6 \times 10^{-3}$ dpa/s, $\vec{n} \sim [110]$, and (a) $\vec{g} = [002]$ and (b) $\vec{g} = [220]$. The dark inner zone is the irradiated area covered by a surface film of Ni_3Ge. The outer circular zone contains a high density of discrete Ni_3Ge particles that result from the radial outflow of Ge from the irradiated zone.